9950-688

DOE/JPL -956046-82/3
Distribution Category UC-63
Report #4

PROCESSED-INDUCED DEFECTS IN EFG RIBBONS

(NASA-CR-169205) PROCESSED-INDUCED DEFECTS IN EFG RIBBONS (Cornell Univ., Ithaca, N. Y.) 14 p HC A02/MF A01 CSCL 10A

N82-29724

Unclas
G3/44 28594

May 1982

JPL Contract No.956046

by

B.Cunningham and D.G.Ast

Materials Science and Engineering
Bard Hall, Cornell University
Ithaca, New York 14853

The JPL low-cost solar array project is sponsored by the U.S. Department of Energy and forms part of the Solar Photovoltaic Conversion Program to initiate a major effort toward the development of low-cost solar arrays. This work was performed for the Jet Propulsion Laboratory, California Institute of Technology by agreement between NASA and DOE.

PROCESS-INDUCED DEFECTS IN EFG SILICON RIBBONS

B. Cunningham and D.G. Ast
Department of Materials Science and Engineering
Cornell University, Bard Hall
Ithaca, N.Y. 14853

Abstract

The defect structure of processed edge defined film-fed growth (EFG) silicon ribbons has been studied using a variety of electron microscopic techniques. Comparison between the present results and previous studies on as-grown ribbons has shown that solar cell processing introduces additional defects into the ribbons.

The creation of point defects during high temperature phosphorus diffusion induces dislocation climb, resulting in the formation of dislocation helices in the diffused layer.

The base regions of the processed ribbons contain low-angle tilt boundaries which are formed during processing. Small precipitates, ∿20nm in size, are found at the low-angle boundaries. In addition, larger precipitates, ∿1μm in size, have been identified. Possible formation mechanisms for these precipitates are discussed.

Introduction

Silicon ribbons grown by the edge defined film-fed growth (EFG) technique are currently being used as substrate material for photovoltaic cells (1). These ribbons generally contain high densities of structural defects, most of which act as efficient minority carrier recombination centers. As-grown EFG ribbons have been studied in considerable detail (e.g. 2,3) and are found to contain first order twin boundaries, higher order twin boundaries and lattice dislocations. Large temperature gradients in the ribbons and temperature fluctuations across the solid-liquid interface are responsible for the generation of most of the structural defects. So far it has not been possible to eliminate these defects by altering the growth conditions.

Carbon concentrations in EFG ribbons are $\sim 10^{18}$ atoms/cm^3, typically a factor of ten or more higher than those in Czochralski single crystal silicon. The influence of such a high carbon content on the electrical properties and defect structure of EFG ribbons is not well understood. Oxygen is also present since CO/CO_2 is introduced into the die area. It is known that during annealing of Czochralski silicon, carbon-oxygen complexes are formed (4), and that carbon can provide nucleation sites for oxygen precipitation (5). The

processing time of EFG ribbons is short ∿30 mins, compared to the times at which Czochralski silicon is annealed in precipitation studies. The high supersaturation of carbon in EFG ribbons (i.e. a large driving force for precipitation) and short diffusion time favor the formation of numerous, but small precipitates.

Experimental

The growth of EFG ribbons is described in ref. (1). The processing of the ribbons was performed by Mobil Tyco Solar Energy Corporation. A phosphene (PH_3) gas diffusion at 950°C for 30 mins was used to produce a shallow p-n junction about 0.5μm below the ribbon surface.

Samples were selected at random from several processed ribbons. Discs, 3mm in diameter, were removed from the ribbons and ion beam milled to a thickness suitable for electron microscopy, typically <1μm. Specimens were milled from the backside only to study the diffused region, and from both sides to study the base region. Electron microscopic observations were carried out on a Siemens 102 transmission electron microscope (TEM) and on a JEOL 200CX, scanning transmission electron microscope (STEM) equipped for x-ray energy dispersive spectroscopy (EDS). Non-dispersive energy spectroscopy was carried out on a JEOL 733 scanning electron microscope (SEM).

Results

a) Diffused region

Figure 1 shows TEM micrographs of dislocation helices situated in the diffused region of an EFG ribbon. Dislocation helices have never been observed in as-grown ribbons, but have previously been observed in processed semiconductor devices (6), where they were ascribed to the absorption of diffusion created interstitial point defects. The helix shown in Figure 1(a) is typical of those found in the thicker regions of TEM foils. The abrupt change in the direction and helical content of the dislocation, may reflect a gradient in the point defect concentration. Figure 1(b) was taken from a thinner part of the foil and clearly shows the helical nature of the dislocations. It was expected that misfit dislocations would be seen in some of the foils milled from the backside. These misfit dislocations are observed after phosphorus diffusion in single crystal silicon, but none were observed in the present study. In the samples milled from the backside only, dislocation helices were the only defects which were identified as originating from the diffusion process.

b) Base region

The following section describes the defect structure in the base region of processed EFG ribbons.

Figure 2 shows STEM and secondary electron images (SEI) of large precipitates, ∿1μm in size, in an EFG silicon ribbon. The SEI contrast from the arrowed precipitate in figure 2(b) indicates that it is completely embedded in the matrix. TEM analysis shows that the precipitates are surrounded by dense dislocation tangles, figure 3. Figure 4 is a typical x-ray spectrum from one of the precipitates and shows that they contain several metallic impurities such as Fe, Mo, and Ti. The Cu peak is due to scattering from the specimen support grid. Note that the Fe peak is the largest impurity peak of the EDS spectra. Non-dispersive x-ray analysis showed that in addition to the above impurities, the precipitates also contained a large amount of carbon. The precipitates described above have been observed only occasionally in processed ribbons, and it is not certain if they form during processing. The precipitates have never been observed in as-grown ribbons, but it is possible that they were not detected because of their low concentration.

TEM micrographs of several low-angle tilt boundaries are shown in figures 5-12. These boundaries invariably have a <0 1 1> tilt axis, which do not normally coincide with the <0 1 1> surface orientation of the ribbons.

Figure 5 shows a boundary with a nominal 0.5° tilt, in which intrinsic (I) and extrinsic (E) dislocations have been labelled. The intrinsic dislocations lie along the tilt axis and are the dislocations which take up the misorientation between the grains. The extrinsic dislocations are lattice dislocations which have slipped into the boundary. Two types of dislocation nodes are formed as a result of dislocation interactions and these can be seen more clearly in figure 6. The dislocations are out of contrast in figure 6(b) and contrast from the stacking faults of dissociated dislocations and dissociated nodes is observed. Small precipitates, ~20nm in size, have been identified in the boundary, figure 7. The Moire fringes in the precipitates allow them to be detected fairly easily. Figure 8 is a higher magnification micrograph of the area shown in figure 6. The dislocation nodes, N, contain precipitates, while no precipitates are observed at the dissociated nodes, D. The precipitates shown by the arrows lie on dislocation segments between nodes. The above observations indicate that the precipitation process is heterogeneous. The precipitates are too small to obtain x-ray spectra and attempts to obtain micro-diffraction patterns have so far been unsuccessful.

Figure 9 is a TEM micrograph of a 4° tilt boundary and the intrinsic dislocations are, therefore, much closer spaced than those comprising the boundary in figure 5. Figures 10 and 11 show enlarged regions of the boundary, taken with different diffraction conditions. Extrinsic dislocations can also be seen in this boundary. The intrinsic dislocations are only ∿5nm apart and it is unlikely that precipitation would occur on a scale which could be observable by TEM techniques.

Many boundaries of the types discussed above have been observed in processed EFG ribbons. All of the boundaries have <0 1 1> tilt axes with tilt angles up to $\sim 5°$.

A recent observation has provided additional evidence that the low-angle tilt boundaries are formed during processing. Figure 12 is a TEM micrograph of what appears to be a tilt boundary in an earlier stage of formation than those shown in figures 5-11. Dislocation dipoles are visible and many of the dislocations contain either periodic kinks or jogs, implying the adsorption of point defects.

Discussion

a) Introductory remarks

The inhomogeneous distribution of defects in EFG ribbons together with the fact that only very small volumes can be investigated in the transmission electron microscope requires that a large number of specimens has to be studied before reliable information can be obtained on the defect structures. In the present case, many specimens of as-grown and processed ribbons have been studied and conclusions about process induced defects have been made based on statistical differences observed in the two types of specimens.

b) Diffused region

Development of helical dislocations is linked to the generation of point defects during PH_3 diffusion. The number of point defects absorbed per unit length of the dislocation is given by (7):

$$\frac{N}{L} = \frac{\pi r^2 b}{\lambda v_a}$$

where r is the radius of the helix, b is the Burgers vector, v_a the atomic volume and $1/\lambda$ is the number of turns per unit length. The sense of the helix can be analyzed to decide if vacancies or interstitials are absorbed (8); such an analysis was carried out in (6) with the result that the point defects introduced during phosphorus diffusion were interstitials.

The chemical potential $\bar{G}$ of the point defects in equilibrium with a helix is within the framework of the line tension concept, inversely proportional to $\sqrt{4\pi^2 r^2+\lambda^2}$ (7). An analysis of the different section of the helix in Fig. 1b along these lines indicates that $\bar{G}$ in the lower part of the helix is about a factor ~ 2 lower; i.e. that the point defect concentration is roughly $\sim 1/3$ of that in the upper part.

The absence of TEM evidence for diffusion induced misfit dislocations is not understood at present. It is possible, but unlikely, that the failure to detect misfit dislocations is an artifact of the specimen preparation.

The factors governing the generation of misfit dislocations have been studied in detail (see for example ref. [9]). Experimentally, one finds that high doping levels of P do not generate misfit dislocations when one simultaneously dopes with As (9). The mechanism for suppression is not, as one may suspect, strain compensation (P has a smaller and As has a larger covalent radius than Si), but rather suppression of dislocation motion and trapping of point defects (9). It is conceivable that C plays a similar role, for example by solute drag on dislocations, but more experimental information is required before this question can be decided.

c) Base region

The origin of the large precipitates is unknown at present. Because of their relatively rare occurrence, it is not possible to state unambiguously that they are process induced (although never observed in unprocessed EFG, they may have been absent in the small areas investigated by TEM).

The precipitates may have been formed in the melt, in which case their melting point must be higher than ~1410°C, the melting point of Si. The melting point of SiC is 2830°C and that of FeSi is 1410°C (10). Thus it appears likely that stable Si-C-Fe precipitates can be formed in the melt.

Alternatively, we consider the case that the precipitates may have been formed in the solid during processing. In this case an estimate of the diffusion required to generate micro-meter sized particles shows that the particles cannot have formed by bulk diffusion. The particles are, however, surrounded by a dense network of dislocations (Fig. 3) which extends to about 5μm from the particle center. If pipe diffusion occurred, this network of dislocation could conceivably collect and transport sufficient C to form Si-C-X particles at the processing temperatures and time. Thus, although formation in the liquid is more likely, formation in the solid cannot be ruled out with certainty.

The particles appear to act as gettering centers for transition metals, such as Mo, which likely originates from the heat shield from where it is transported as volatile oxide to the ribbon. Cl, which has also been identified, can be traced to the Cl bakeout of the graphite dies.

Since transition metals reduce solar cell performance, formation of these precipitates is likely beneficial.

The small angle boundaries are almost certainly formed during processing. The formation is not linked to the P diffusion since the networks are formed far away from the junction. Unprocessed ribbons contain high internal stresses which are partially relieved by dislocation motion and multiplication at the temperatures required for processing.

It appears that the boundaries are formed by this process. Dislocation nodes in these boundaries offer nucleation sites for precipitation. Note that C does not seem to segregate to stacking faults (Suzuki segregation) since the extended nodes do not act as nuclei. This observation is in agreement with the general rule that elements which increase the energy difference between the staggered and eclipsed bond configuration will not segregate to stacking faults. C with its higher bond strength and bandgap is expected to increase this difference.

If the precipitates are SiC, they contain about $5 \cdot 10^4$C atoms. Since the bulk C content is $\sim 1 \cdot 10^{18}/cm^3$, formation of the small precipitates requires diffusion over distances of $\sim 0.4 \mu m$ at the processing time ($\sim$30 min) and temperature ($\sim$950°C), or a diffusion coefficient of roughly $1 \cdot 10^{-12} cm^2/sec$. The diffusion coefficient of C at 950°C is $\sim 1 \cdot 10^{-12} cm^2/sec$ (11) and the observed size of the precipitates is, therefore, compatible with the hypothesis that they are formed during processing and that they are related to C. Oxygen may also be involved since the diffusion coefficient (about $1 \cdot 10^{-11} cm^2/sec$ at 950°C [11]) and bulk concentration ($0.3 - 1.2 \cdot 10^{18}/cm^3$ [12]) are roughly similar to carbon. The influence of the small precipitates on the efficiency of solar cells fabricated from EFG ribbons has not been studied. EFG based cells behave somewhat differently from standard single crystal cells in that the electrical properties depend on the intensity of the incident light. A study of the relation between the electrical properties and the size and density of the small precipitates is planned.

Conclusions

TEM of processed EFG has identified a variety of defects which are introduced during processing; i.e. point defects, large precipitates, and small, heterogenously nucleated precipitates. The latter form at dislocation nodes of process induced sub-boundaries with <0 1 1> tilt components. The large precipitates are probably formed in the liquid although pipe diffusion models can be constructed to account for their formation in the solid. The size of the small precipitates is compatible with estimates that their formation is controlled by the bulk diffusion of C or O. Undissociated dislocation nodes in sub-boundaries, formed during processing, act as nucleation sites for the precipitates.

Acknowledgment

This research was sponsored by JPL under Contract No. 954852 and by DOE under Contract No. DE-AC02-76ER02899. The specimens, which were grown by Mobil-Tyco, were supplied by JPL as part of the LAS program. The Materials Science Center at Cornell University provided facilities for research.

References

1. J.P. Kalejs, B.H. Mackintosh and T. Surek, J. Cryst. Growth, 50, 175 (1980).
2. B. Cunningham, H.P. Strunk and D.G. Ast, Appl. Phys. Lett., 40, 237 (1982).
3. H.P. Strunk, B. Cunningham and D.G. Ast, "Defect Structure of EFG Silicon Ribbons," JPL/DOE Report No. 954852-6 (1980).
4. G.S. Oehrlein, J.L. Lindstrom and J.W. Corbett, Appl. Phys. Lett., 40, 241 (1982).
5. W.K. Tice and T.Y. Tan, Defects in Semiconductors, eds. J. Narayan and T.Y. Tan, North-Holland Inc. (1981).
6. H.P. Strunk, V. Goesele and B.O. Kolbesen, J. Microsc., 118, 35 (1980).
7. J.P. Hirth and Y. Lothe, Theory of Dislocations, McGraw Hill, 576 (1968).
8. Ibid, p. 571
9. T. Yonezewa et. al., in Semiconductor Silicon eds. R. Huff and E. Sirtl, Proc. 77-2, Electrochemical Soc., Inc., P.O. Box 2071, Princeton, N.Y. 08540, 658 (1977).
10. W.R. Runyan, Silicon Semiconductor Technology, McGraw Hill, 247 ff (1965).
11. Ibid, p. 185 ff
12. J. Hanoka, private communication

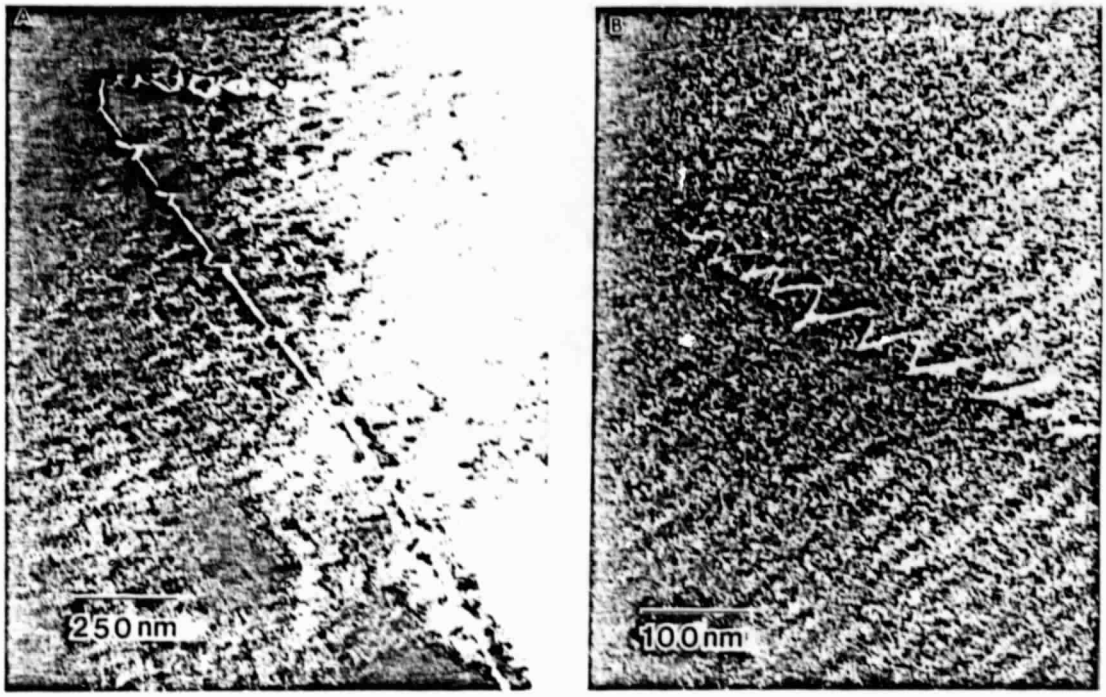

Figure 1. Dislocation helices in the diffused region of an EFG ribbon.

Figure 2. a) STEM and b) secondary electron images of large precipitates in the silicon matrix.

Figure 3. TEM micrograph of the dislocation tangle surrounding a precipitate

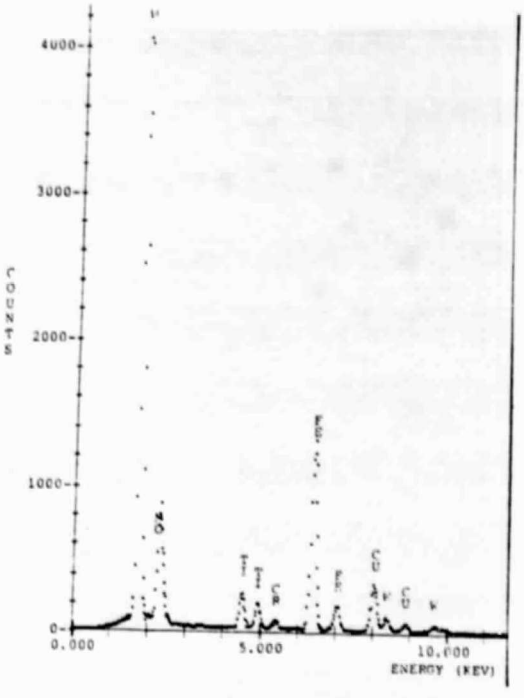

Figure 4. X-ray energy dispersive spectrum from one of the precipitates shown in figure 2.

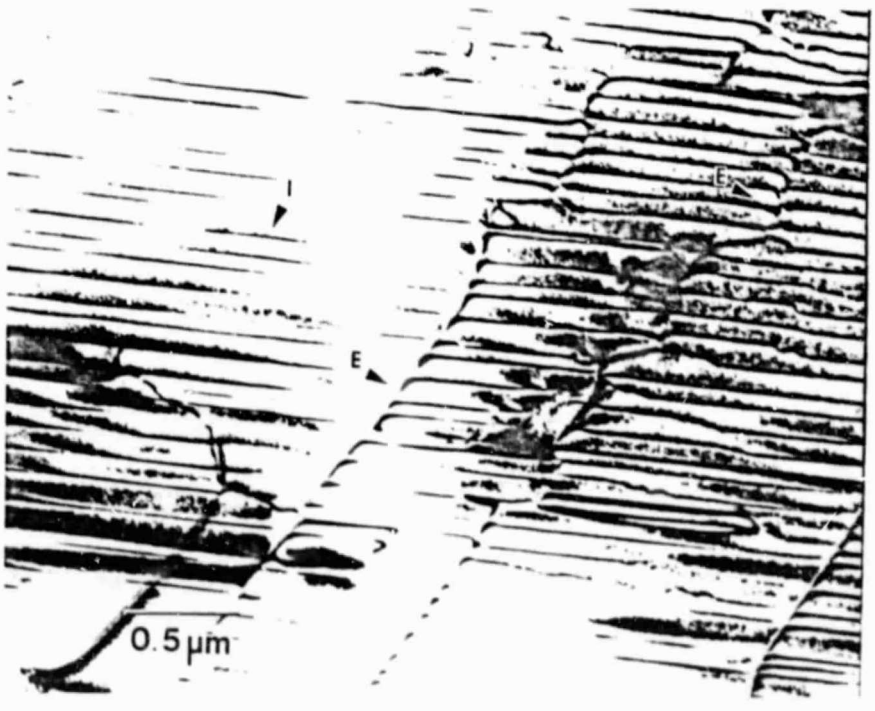

Figure 5. Low angle tilt boundary. Intrinsic (I) and extrinsic (E) dislocations are shown.

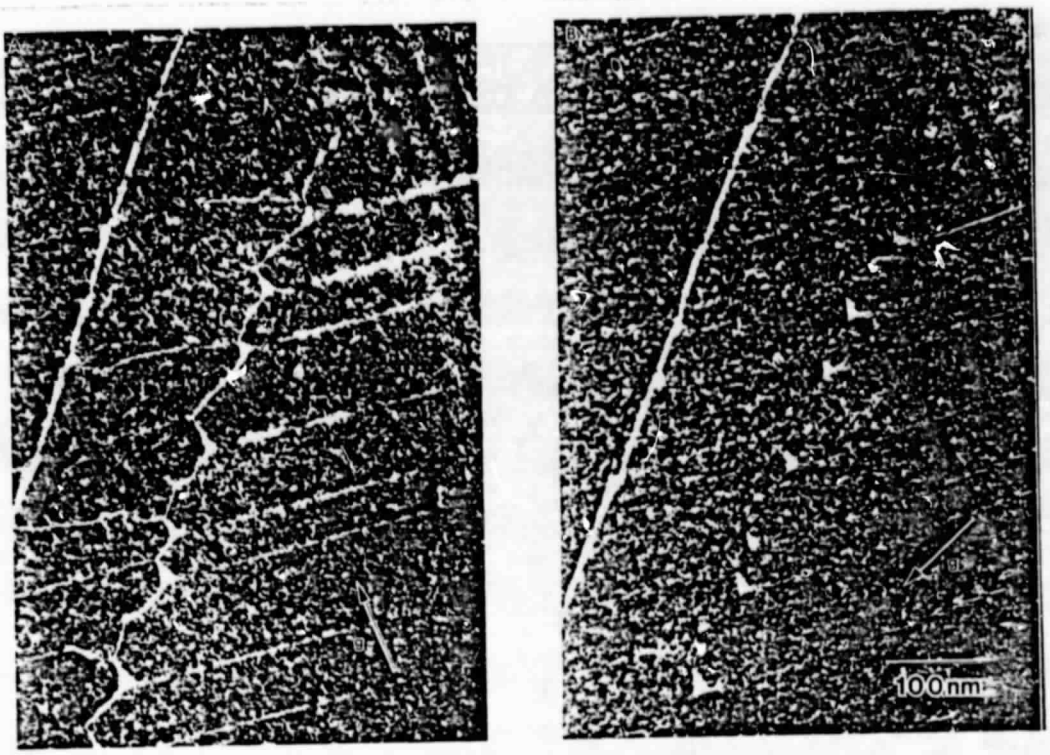

Figure 6. Weak-beam micrographs showing two types of dislocation nodes in a low-angle boundary. g=diffraction vector

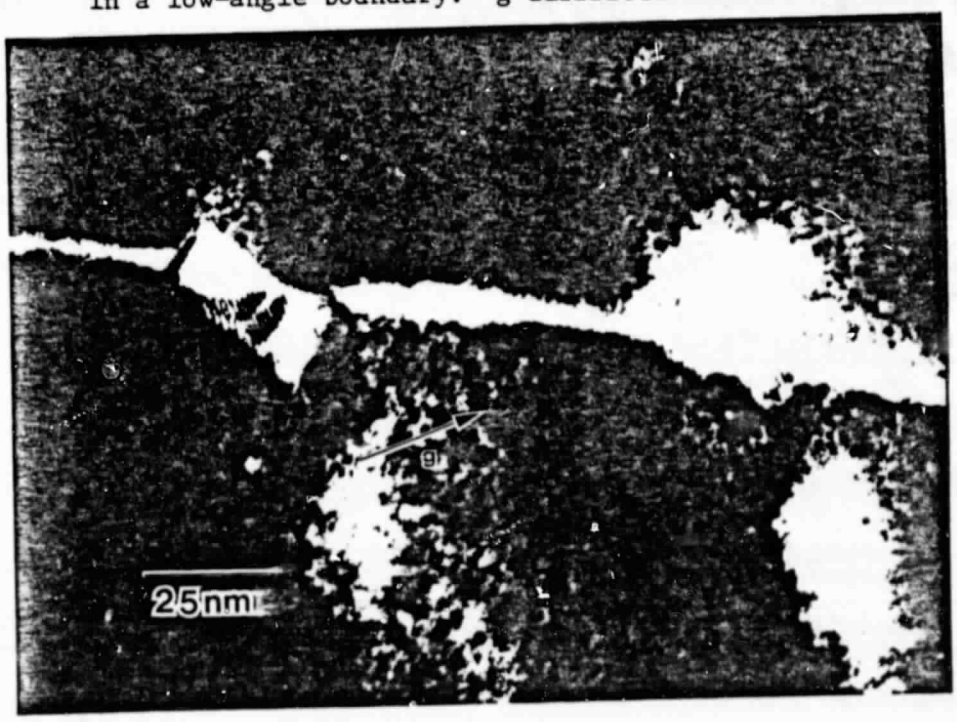

Figure 7. Precipitates at dislocation nodes in low-angle boundary. g=diffraction vector

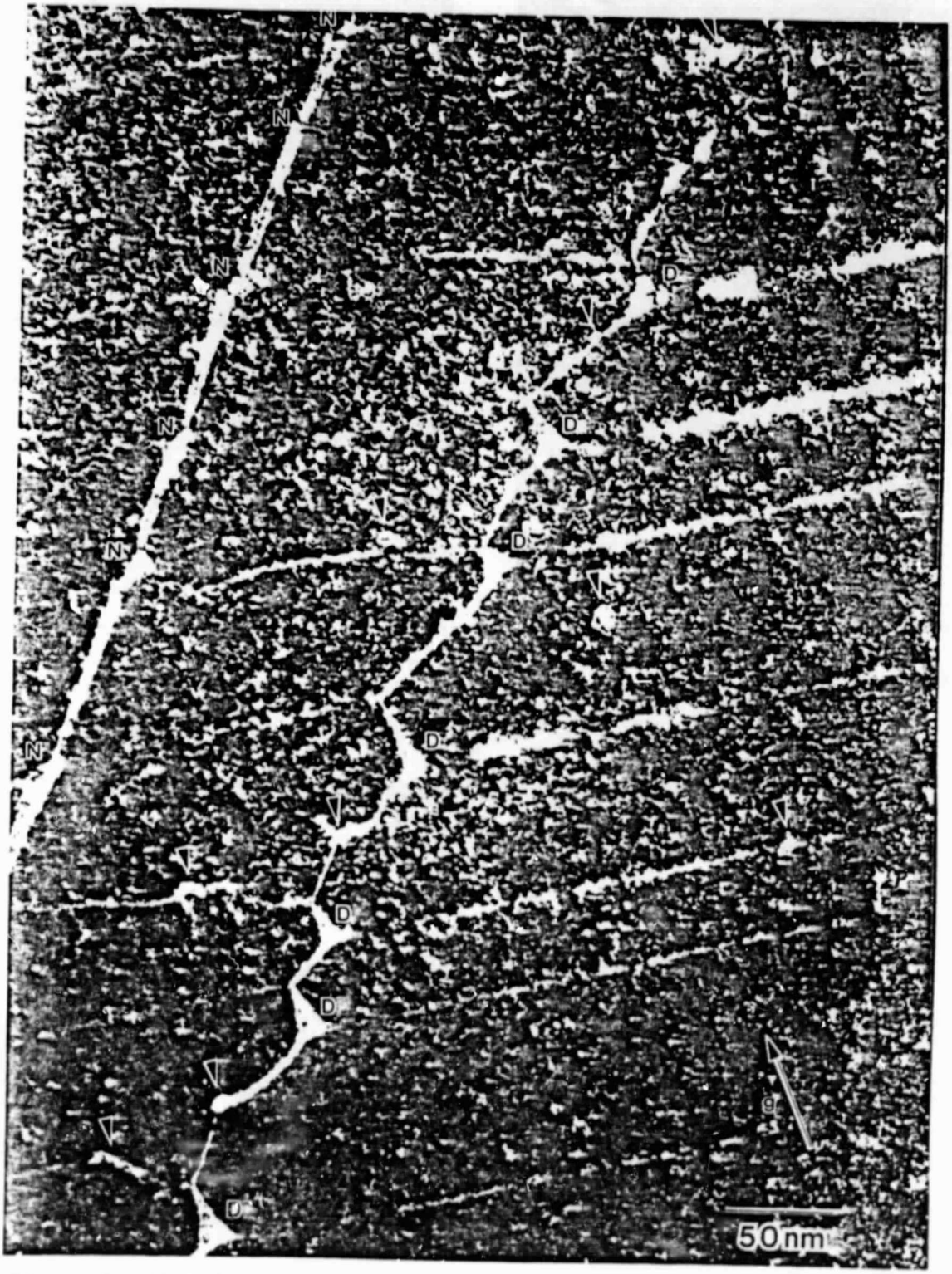

Figure 8. Weak-beam micrograph showing precipitation at a low-angle boundary. See text for further details.

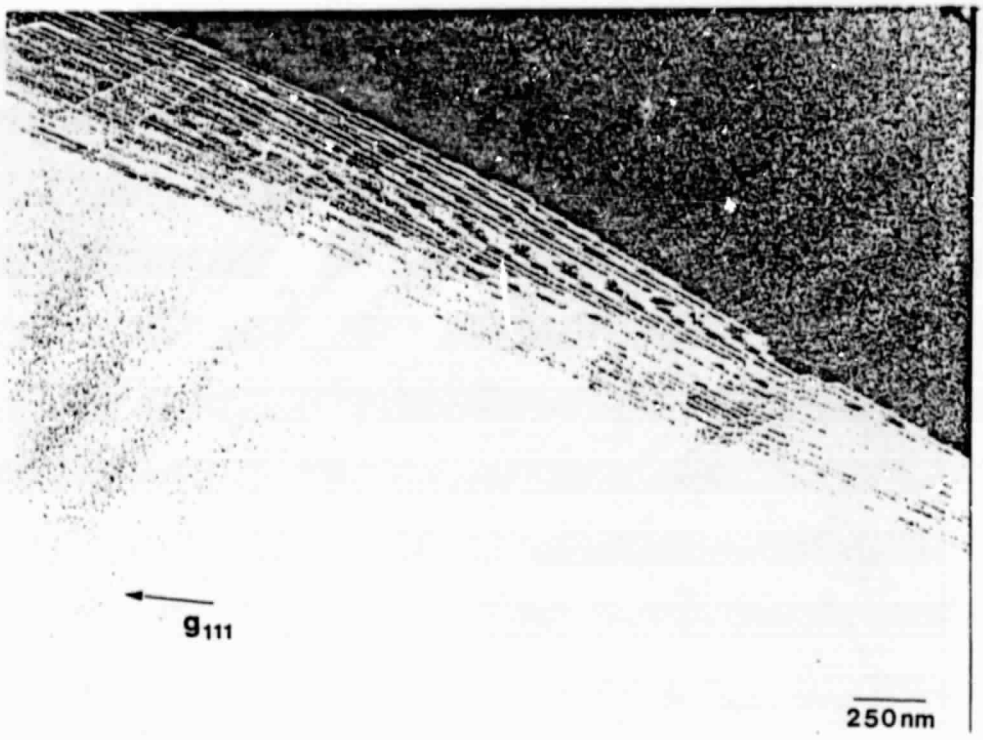

Figure 9. 4° tilt boundary in processed ribbon.

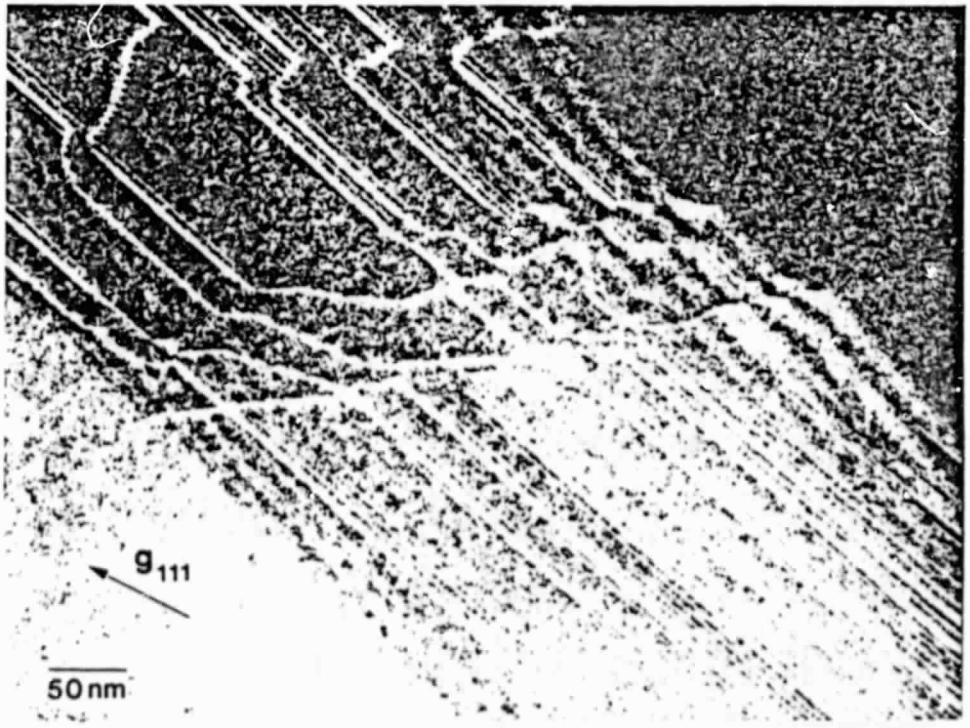

Figure 10. Higher magnification micrograph of boundary shown in figure 9.

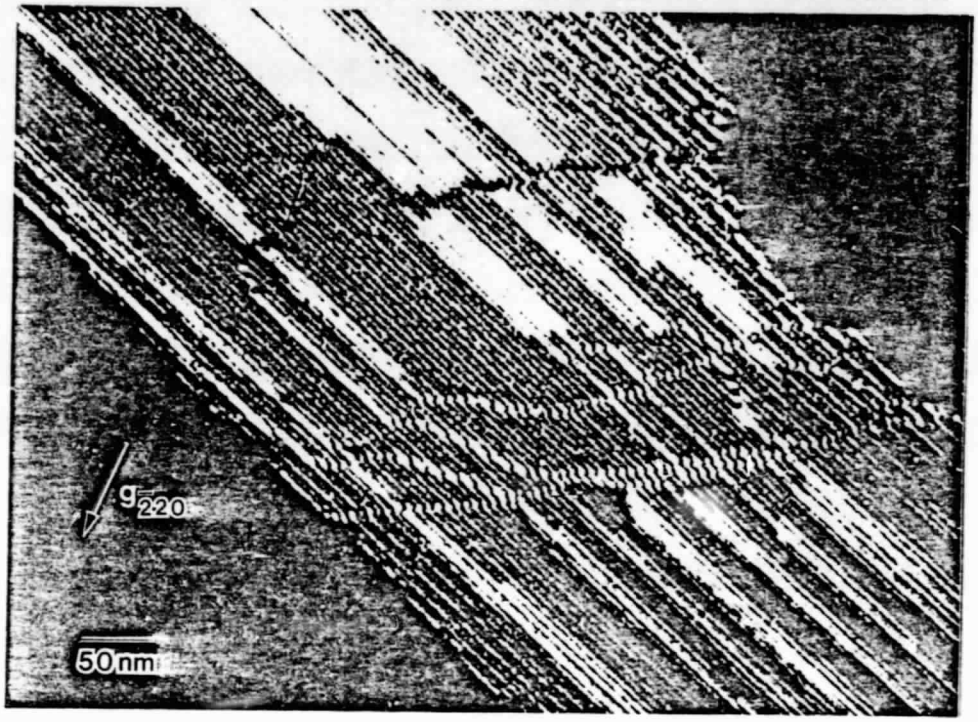

Figure 11. Same area as figure 10 imaged with different diffraction vector.

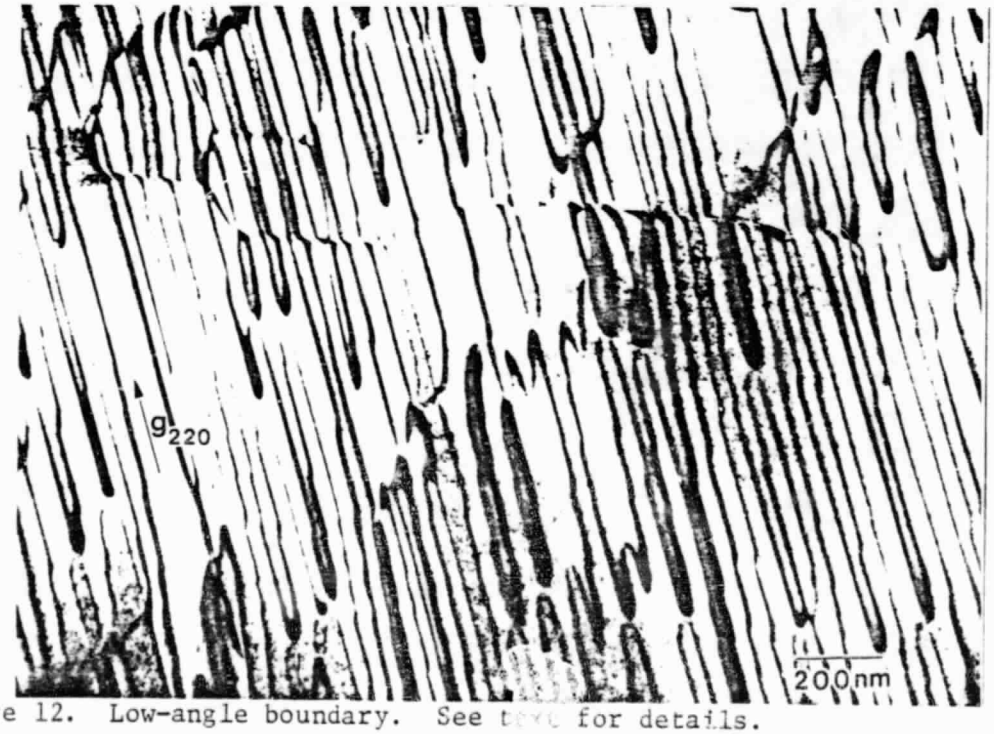

Figure 12. Low-angle boundary. See text for details.